UAV Ground Impact Mitigation for Safer Flight Response

Andrew Poissant, Lina Castano, and Huan Xu, *Member, IEEE*

Abstract—As Unmanned Aerial Vehicles (UAVs) become more widely used, there is a growing need for safer flight control software that allows UAVs to understand and autonomously react to various flight anomalies. Decision-making software should allow the aircraft to perform tasks such as detection and avoidance, as well as respond to critical failures mid-flight, without input from a human operator. This paper develops a ground impact and hazard mitigation (GIHM) decision-making module that integrates the following: (1) consideration of engine and control surface failure flight modes, (2) generation of feasible ground impact footprints based on glide equations, (3) selection of safest response ground impact sites based on a high resolution LandScan USA population dataset, and (4) controlled descent to a selected site. For a sample population distribution, integration of GIHM with standard UAV flight software shows a reduction of 23.014 casualties per 100,000 flight hours compared to the flight software without GIHM. A 97.5% reduction in fatalities per flight hour resulted from incorporating this module, which brings UAVs closer to being safe enough to be integrated into the National Airspace System (NAS).

Index Terms—Reachable ground footprint, LandScan, safer UAV response, hazard mitigation, collective risk.

I. INTRODUCTION

Software for the control of Unmanned Aerial Vehicles (UAVs) has become increasingly sophisticated and elaborate over the past decade. The main focus on such software, however, has been on automatic control, not autonomous control [1]. Automatic control provides the necessary automation of nominal operational control, while autonomous control must allow for a level of autonomy that predicts and responds to any event and condition [1]. There remains a critical need for fully developed safety software within the UAV system architecture that can make informed decisions in the presence of flight anomalies [2]. This work presents a decision-making module that is able to respond to critical flight anomalies and minimize hazards to other aircraft and the general population.

Two major hazards associated with UAV operations are collisions between the UAV and a Conventionally-Piloted Aircraft (CPA), and impact of the UAV with terrain, people, or structures [3]. These hazards pose a large risk to the general public, with casualties being a worst-case scenario. UAVs can have accident rates as high as 32 accidents per 100,000 flight hours, 32 times higher than the accident rates for small general aviation aircraft, and 3,200 times higher than large airliners [2]. With UAV accident rates significantly higher than that

A. Poissant is with the Institute for Systems Research, University of Maryland, College Park, MD 20742 USA e-mail: apoissant95@gmail.com.

L. Castano is with the Aerospace Engineering Department, University of Maryland, College Park, MD 20742 USA e-mail: linacs@umd.edu.

H. Xu is with the Aerospace Engineering Department and Institute for Systems Research, University of Maryland, College Park, MD 20742 USA e-mail: mumu@umd.edu.

of CPAs, there is a clear need for additional safety measures for UAV control software and hardware before they can be integrated into the National Airspace System (NAS).

A 2012 Congressional Research Service (CRS) Report detailed the required technology and standard procedures for safe UAV control software, requiring UAVs to have technology and standard procedures for sensing and avoiding other air traffic under all possible scenarios, including loss of communications [4]. For instance, the UAV must be able to autonomously return home or determine a safe path to crash [4]. Furthermore, as detailed in [5], all UAVs must operate in restricted airspace or at extremely low altitudes, which increases the risk of collision. In order to integrate UAVs into the NAS, airborne safety must be ensured by avoiding midair collisions and guarding against ground impact in the event of an impending crash. The contribution of this paper is the development and integration of a module that guards against casualties due to ground impact. It focuses on the effects of critical vehicle failure modes and the vehicle's ability to reach a safe crash location.

Characterizing failure modes is an important aspect in guarding against ground impact. If a flight anomaly and the effect of that anomaly on the aircraft states are known, then the aircraft's reachable ground footprint can be calculated. The failure mode determines the capabilities and maneuverability of the aircraft, which must be considered when developing ground footprint models in order to reduce its hazard on the ground. For UAVs, these modes may include actuator failures, sensor failures, engine malfunction, loss of radio link and GPS, as well as structural damage such as a broken propeller, wing, etc., caused by unanticipated flight events [6].

This paper focuses on two particular categories: engine malfunction and actuator failures. We investigate engine malfunctions because of their prevalence as one of the root causes of UAS failures [7]. Actuator faults are studied as they contain several moving parts and are among the least reliable components on a UAV. Because actuators are connected to aerodynamic control surfaces, actuator faults directly affect the flight dynamics of the UAV. Actuator failures can lead to significant loss in controllability of the aircraft and, eventually, catastrophic failure [8].

A wide body of literature exists in assessing the collective risk that faulty UAVs pose, both in-air [9][10][2] and on the ground [9][10][11][12][13][14]. In particular, ground risk models have the following general components: failure mode, impact location, recovery, stress, exposure, incident stress, and harm [15]. Of these components, our work entails the following: failure modes, ground impact location, stress caused by fatalities and exposure via population data. Previous works have developed impact location models such as ground footprints and geometries of reachable areas [15]. The work

presented in [16] investigated the ability of a fixed-wing aircraft to glide to a designated emergency landing area. The authors in [3] and [17] use 6 degree-of-freedom models to develop ground impact models for determining the reachable ground envelope of UAVs, and research in [18] developed an emergency no-thrust flight trajectory plan. None of these works, however, incorporate flight control software into these models. They furthermore do not examine collective risk profiles that consider high resolution population data and reaction protocols for real-time implementation, as our work does. Accurate population data can be used to further understand the collective risk a UAV poses to a given area. Previous work has used census data or local tax data [9][10][11][12][13]. However, such information can be hard to acquire and can be largely unrepresentative of the true population count for a given area. The work of [19] used demographic population data for entire cities and states to generate population data for use in developing collective risk profiles. Using data at such large scales can result in significant uncertainty if finer resolution population data is required. For this reason, population data based on LandScan USA data was used in our work to obtain accurate population data. The LandScan USA dataset represents ambient population at 90 m resolution anywhere in the United States [20]. In previous literature, Landscan data has been used for mapping global impacts from climate change, building and evaluating population density models, mapping spread of dangerous diseases, and much more [21][22][23]. However, to our knowledge, LandScan data has never been used for the purpose of determining the lowest risk ground impact point for a UAV experiencing a hazardous flight anomaly.

Given the previous related work described above, there is still a need for an all-encompassing ground impact mitigation system. The contribution of this paper, which builds on our previous work [24], is the integration of a novel ground impact and decision making model with a high resolution population dataset to provide high accuracy collective risk profiles for safer UAV response. **Compared to [24], this paper provides feasible ground impact footprint equations and fault mitigation techniques for three new fault modes, in addition to simulation results and analysis for these new fault modes**. Furthermore, this work integrates with a high-fidelity flight software that includes a mission plan, a path planning module, 6-DOF aircraft model, and flight controller. Integration of the reachable footprint and risk distribution profiles with the flight control software demonstrates the potential real-life implications of this work. Simulations demonstrate how UAVs react to these critical flight anomalies. We show that with the ground impact and hazard mitigation (GIHM) module developed in this work, fatalities per flight hour were decreased by 97.5% in the proposed population scenario.

The remainder of this paper is structured as follows: Section II describes the architecture and requirements of GIHM, Section III develops the feasible ground impact footprint models, Section IV details the fault modes and safest response, and Sections V and VI present a case study, discussion, and conclusions.
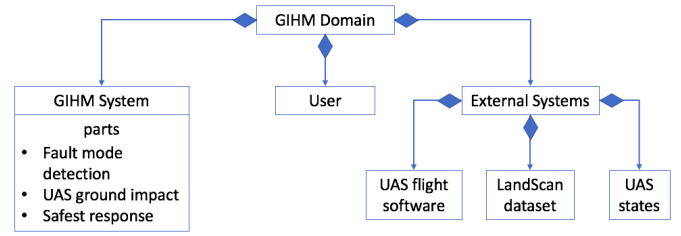

Fig. 1. GIHM system domain definition BDD. This establishes the domain of the system, which contains the GIHM system, user, and external systems.
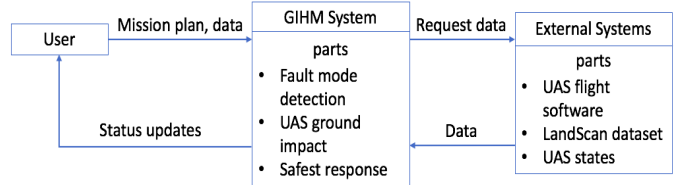

Fig. 2. GIHM context level IBD. This shows how the system interacts with its user and external systems.

II. CONTEXT-LEVEL ARCHITECTURE AND REQUIREMENTS

Before beginning development of GIHM, we provide architectural artifacts and requirements. One of the biggest challenges in developing safer UAV flight control software is vague and ambiguous requirements and lack of systems engineering diagramming. Specific requirements and architectures are needed when tackling autonomous decision making [25].

A. Context-Level Architecture

We begin by presenting the block definition and internal block definition diagrams for GIHM. Fig. 1 shows the system domain block definition diagram (BDD) for the ground impact and hazard mitigation (GIHM) module. The diagram provides a definition of the system and its environment in terms of the principal elements. GIHM is comprised of three elements: fault mode detection, UAV ground impact, and safest response. The GIHM system interacts with its external systems, which consists of the UAV flight software, flight states, and the LandScan population dataset. The user initiates the flight by entering the mission plan in the form of waypoints and uploads the area of operation data from LandScan.

Fig. 2 details the context level internal block diagram (IBD) for GIHM. This IBD identifies how the system interacts with its user and external systems, its system boundaries, and state flows (data exchanged between blocks) between the system of interest, user, and external systems. The state flows for GIHM include the mission plan in the form of waypoints, UAV states sent to GIHM (e.g., GPS coordinates, airspeed, roll, pitch, and yaw), and updated UAV states sent to the user. While GIHM was used fully autonomously in simulation (no input from the user after flight initiation), the level of autonomy can be adjusted to allow the user to be involved in the decision to use the new priority waypoints generated by GIHM. The system context BDD also shows that the UAV flight software sends data real-time to GIHM and GIHM determines if there is a critical flight anomaly with the goal of minimizing its ground

impact. Before flight, the user selects from LandScan data the area of operation for the UAV and uploads that data for use in case of a flight anomaly. From this data, GIHM can send new waypoints to the UAV flight software, where the software executes the new mission plan.

B. System Requirements

Having presented two of the key architectural artifacts, we now develop the requirements for GIHM. To do this, we must identify a metric to quantify the safety of a UAV. Collective risk is the most commonly used metric in UAV ground models because it describes the aggregate risk to a population [3]. This metric has units of casualties per flight hour and shall be reduced by using UAV flight control software with GIHM. Results are generally dependent on the specific population scenario. GIHM is designed to reduce the number of casualties from UAV operations, and thus its collective risk. To accomplish this, the following system requirements need to be established where GIHM shall:

- Determine the UAV's flight states (e.g., GPS coordinates, airspeed, roll, pitch, yaw)
- Predict the feasible ground impact footprint (FGIF),
- Use the FGIF to extract local population count map from LandScan data,
- Process LandScan local population count map to extract lowest hazard zones as a candidate for landing,
- Select the safest hazard response,
- Generate a revised UAV flight plan to implement safest response.

When an anomaly is detected by the decision making module, GIHM must analyze the anomaly and determine which fault mode the aircraft is in. A fault is defined as an unallowed deviation of at least one characteristic property of the system from its standard operating condition [26]. Data driven fault detection methods include checking limits on signal values and data trends. One approach is to detect an anomaly by comparing current measured UAV states to expected ranges of vehicle states, (e.g., airspeed, thrust, Euler angles, angular rates, system components and actuator deflections) [26]. If any of the values are deemed to be out of their expected operating range, a corresponding fault mode is diagnosed. One of the indicators of an inoperative engine is a sustained decrease in thrust, causing the aircraft to deviate from its course and may pose a safety threat to nearby population in urban and suburban areas. For this work, the following four fault modes are considered:

1) Engine failure - UAV engine malfunction, resulting in no thrust.
2) Engine and rudder failure - UAV engine and rudder control surface failure. Rudder control surface is stuck at the deflection it had during time of the fault.
3) Engine and elevator failure - UAV engine and elevator control surface failure. Elevator control surface is stuck close to trim deflection. Trim value was chosen, as opposed to some value above trim, because it is of less severity and there is still some level of controllability over the new dynamics caused by the fault [27]. Additionally,

this work does not consider any fault reconfiguration or reallocation methods.
4) Engine and ailerons failure - UAV engine and ailerons control surfaces failure. Ailerons control surface is stuck close to trim deflection, for similar reasons as those stated in 3).

With the states of the UAV known, and after detecting and diagnosing a flight anomaly, GIHM then predicts the FGIF using gliding flight equations and current UAV states. The local population data from LandScan is extracted, which is preloaded by the user before flight is initiated. Population data is then processed, with the lowest hazard zones identified. With the lowest hazard landing areas known, GIHM selects the safest hazard response. The safest response consists of a new set of waypoints that the UAV follows to crash, assuming a safe landing zone is unfeasible. This response is a function of the collective risk in the identified reachable zone and whether the starting or ending waypoints are within the FGIF. Finally, GIHM sends the new mission waypoints to the UAV flight control software for implementation. Because this work does not focus on landing site determination, the waypoint that GIHM provides can be considered a crash point. This work also doesn't consider effects of winds or turbulence, these are part of future work.

C. GIHM Integration with UAV Flight Software

GIHM interfaces with a 6-DOF flight simulation software of a small, fixed-wing UAV, developed in Matlab/Simulink. Fig. 3 shows how GIHM interfaces with the flight simulation software at a top level. Fig. 4 shows a low level block flow diagram detailing how GIHM processes the system states and outputs crashing waypoints if a fault mode is detected. The UAV states are sent to GIHM, where GIHM determines whether the UAV is experiencing a fault mode.
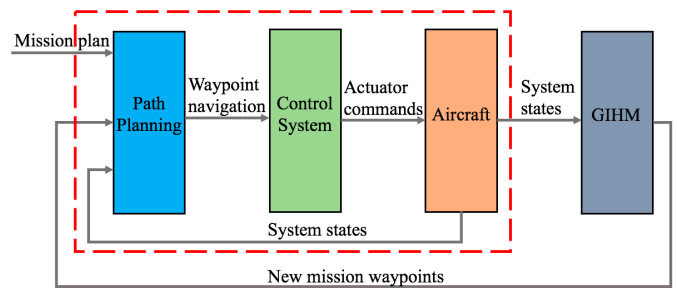

Fig. 3. Top level GIHM integration with UAV flight software. The components inside the dashed red box contain the nominal UAV flight software architecture. GIHM takes the UAV system states as an input and outputs new mission waypoints if a flight anomaly is detected.

In this work, a flight anomaly is detected when the UAV aircraft states are outside of a predetermined nominal range. If a fault mode is detected, GIHM sends back new mission GPS coordinates to the UAV flight control software. These new coordinates replace old mission waypoints.

The standard flight simulation architecture contains a path planning block, control system block, and aircraft block. The path planning block takes the initial 3D mission waypoints and calculates desired values so that the UAV can reach

them. These values go into the autopilot which uses altitude and lateral-directional control for trajectory tracking via PID controllers. It then uses the desired navigation requirements to output actuator commands to the UAV. Finally, the aircraft block, which houses the UAV aircraft model, takes in actuator commands to update the new system states. The aircraft model uses aerodynamic forces and moments, and incorporates environmental factors related to altitude for air density and dynamic pressure calculations.

III. FEASIBLE GROUND IMPACT FOOTPRINT

With the system architecture and requirements established, we now move into model development for GIHM. To fulfill its requirements, GIHM must accurately predict everywhere on the ground the UAV can reach. This is also known as the aircraft's feasible ground impact footprint (FGIF). Gliding equations are used for the FGIF calculations due to the choice of simulating a prevailing engine failure. Table I contains variable descriptions for the gliding flight equations presented in this section. Fig. 5 depicts the axis representation used in development of the FGIF models. Variables d_x and d_y represent displacements in the longitudinal and latitudinal direction, respectively, and d_z represents displacement in altitude. The gliding flight equations were iterated over an aircraft's 360° of maneuverability to obtain a full reachable envelope.

A. Gliding Flight

Calculation of the FGIF requires the vehicle's initial latitude, longitude, altitude, airspeed, roll angle, pitch angle, and yaw angle. These values are obtained from the UAV flight control software. The gliding flight equations are derived from the following equations of motion in the aircraft's longitudinal, lateral, and vertical axis respectively [28]:

$$m\frac{dv}{dt} = -mgsin(\theta) - D + Tcos(\theta), \tag{1}$$

$$mgcos(\theta)sin(\phi) = mv\dot{\psi}cos(\theta)cos(\phi), \tag{2}$$

$$mgcos(\theta)cos(\phi) - L - Tcos(\theta) = -mv\dot{\psi}cos(\theta)sin(\phi), \tag{3}$$

where ϕ, θ, and ψ are roll, pitch, and yaw angle, respectively. $\dot{\psi}$ is the turn rate of the aircraft, m is the aircraft's mass, g is acceleration of gravity, D is drag, and L is lift, and T is thrust. From here we make the following assumption: for an

Fig. 4. Low level block flow diagram for GIHM. Inside GIHM there is a Fault Mode Detector block, FGIF Generation block, LandScan USA Data block, Casualty Expectation Profile block, and Find Lowest Hazard Waypoint block.
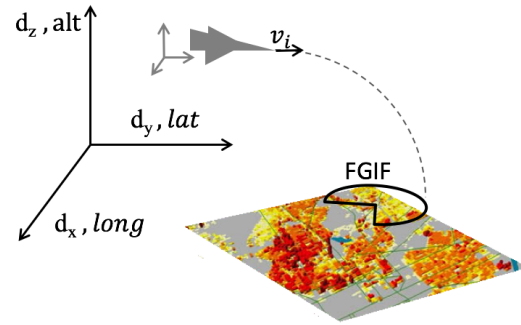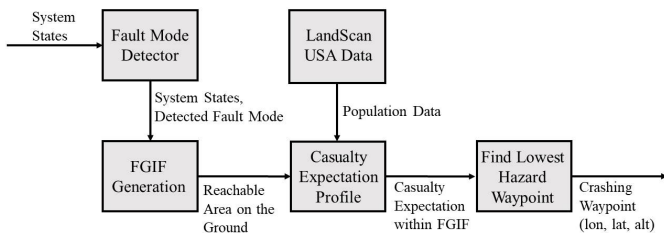

Fig. 5. Depiction of the FGIF and coordinate system. d_x, d_y, and d_z represent displacement in the longitude, latitude, and altitude directions, respectively. The UAV's reachable footprint is represented by the semi-circle labeled FGIF.

TABLE I. Definitions of variables in gliding flight equations.

Variable	Definition
m	aircraft mass
v	airspeed
g	acceleration of gravity
θ	pitch angle
D	drag
T	thrust
ϕ	roll angle
L	lift
ψ	yaw angle
$\dot{\psi}$	turn rate
Δh_{turn}	height loss during the turning phase
L_{arc}	arc length of the circle made by a turn
v_ϕ	airspeed during the turning phase
$v_{s\phi}$	sink rate during the turning phase
v_s	sink rate
R	radius of the circle during the turning phase
$d\psi$	total change in heading
W	aircraft weight
C_D	coefficient of drag
ρ_0	density of air at sea level
S	wing area
C_{do}	profile drag
k	induced drag factor
C_L	coefficient of lift
A_r	wing aspect ratio
C_{L_0}	coefficient of lift at zero angle of attack
C_{L_α}	angle of attack stability derivative
α	angle of attack
$d_{x,t}$	distance traveled in x direction during turning phase
$d_{y,t}$	distance traveled in y direction during turning phase
$d_{x,s}$	distance traveled in x direction during straight level phase
$d_{y,s}$	distance traveled in y direction during straight level phase
D_{glide}	glide distance during straight level phase
h_i	aircraft's initial height before entering gliding flight
d_x	total distance traveled in x direction during gliding flight
d_y	total distance traveled in y direction during gliding flight

engine out case, we set $T = 0$, resulting in gliding flight. If a small glide angle approximation is used (which is the case for most aircraft), the gliding flight equations are simplified to:

$$0 = -mgsin(\theta) - D, \tag{4}$$

$$tan(\phi) = \frac{v\dot{\psi}}{g}, \tag{5}$$

$$mgcos(\phi) - L = -mv\dot{\psi}sin(\phi). \tag{6}$$

Eqs. 4-6 are the three primary equations of motion for gliding flight in the aircraft's longitudinal, lateral, and vertical axis.

B. Footprint Calculation

The footprint consists of all the possible reachable locations on the ground that the aircraft can glide to. This gliding range calculation consists on projecting how far the aircraft can travel during turning and level flight. It is important to note that these calculations require dynamic access to vehicle states, e.g. Euler angles, velocities, as well as aerodynamic parameters from the aircraft model. Fig. 6 shows an illustration of the construction of the footprint, with reference direction due north.

1) Turning phase: To calculate the aircraft's height loss during the turning phase, we use

$$\Delta h_{turn} = L_{arc} \frac{v_{s\phi}}{v_\phi}, \tag{7}$$

where $v_{s\phi}$ is the sink rate of the aircraft in the turning phase, v_ϕ is airspeed during the turning phase, and L_{arc} is the arc length of the circle made by the turn. v_ϕ and $v_{s\phi}$ are calculated using the following equations [16]:

$$v_\phi = vsec^{\frac{1}{2}}(\phi), \tag{8}$$

$$v_{s\phi} = v_s sec^{\frac{3}{2}}(\phi). \tag{9}$$

L_{arc} is calculated using the following equations:

$$L_{arc} = Rd\psi, \tag{10}$$

$$R = \frac{v^2}{gtan(\phi)}, \tag{11}$$

where R is the radius of the circle and $d\psi$ is the total change in heading. $d\psi$ is bounded between $\pm\pi$ to account for an aircraft's ability to turn in the positive and negative directions.

An aircraft's rate of sink, v_s, is the amount of height loss per unit time the aircraft is flying during gliding flight. v_s is a function of the aircraft's drag, weight, and velocity through the following equation [28]:

$$v_s = \frac{Dv}{W}. \tag{12}$$

To calculate drag, we use equations from [29]:

$$D = 0.5C_D\rho_0v^2S, \tag{13}$$

$$C_D = C_{D_0} + \frac{kC_L^2}{\pi A_r}, \tag{14}$$

where ρ_0 is the density of air at sea level, S is the wing area, C_{D_0} is the aircraft's profile drag, and k is the induced
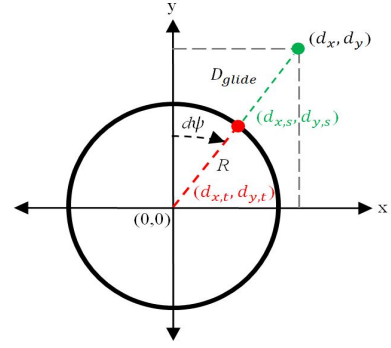

Fig. 6. Glide range geometry representation: The reachable footprint (FGIF) includes points generated in the turning phase and straight level phase flight of the UAV, centered at (0,0).

drag factor, determined by the aircraft wing dimensions, configuration, Reynolds Number and Mach Number. A_r is the aircraft's wing aspect ratio and C_L is the coefficient of lift.

The following equation was used to calculate C_L [30]:

$$C_L = C_{L_0} + C_{L_\alpha}\alpha, \tag{15}$$

where C_{L_0} is the aircraft's coefficient of lift at zero angle of attack, C_{L_α} is the angle of attack stability derivative and α is the aircraft's angle of attack. This equation is valid for small angle of attack. Since the aircraft is not approaching stall conditions, the aircraft's angle of attack will be within the linear region of the angle of attack vs. coefficient of lift relationship.

Once the height loss during the turning phase is calculated, we next determine how far in the x and y directions the aircraft travels during the turning phase ($d_{x,t}$, $d_{y,t}$), which were calculated using:

$$d_{x,t} = Rsin(d\psi), \tag{16}$$

$$d_{y,t} = Rcos(d\psi). \tag{17}$$

2) Straight level phase: The distance traveled during straight level flight ($d_{x,s}$, $d_{y,s}$) is calculated using similar geometry to that of the turn phase:

$$d_{x,s} = D_{glide}sin(d\psi), \tag{18}$$

$$d_{y,s} = D_{glide}cos(d\psi). \tag{19}$$

Total ground distance traveled in the straight level flight, D_{glide} is calculated using the following equation [16]:

$$D_{glide} = (h_i - \Delta h_{turn})\frac{v}{v_s}, \tag{20}$$

where h_i is the aircraft's initial height before entering gliding flight. By adding total distances traveled during the turning and straight level phases, the total distance traveled in each direction can be calculated. This results in the final two equations for distance traveled in the xy directions during gliding flight:

$$d_x = Rsin(d\psi) + D_{glide}sin(d\psi), \tag{21}$$

$$d_y = Rcos(d\psi) + D_{glide}cos(d\psi), \tag{22}$$

where d_x and d_y are the coordinates at the end of the glide, relative to the initial position and heading of the aircraft.

The FGIF is comprised of all of the possible d_x and d_y combinations that the aircraft can reach. It is important to note that for this work it is assumed that there is no wind, which would otherwise have an effect on the gliding performance of a UAV. In addition, the reference direction is adjusted to due east for integration with the flight software (Fig. 3). To this effect, an angle factor of $pi/2$ was added to Eqs. 16-22:

$$d\psi_{east} = pi/2 - d\psi. \tag{23}$$

Finally, it is important to consider whether an aircraft can realistically execute the required turns when finalizing its FGIF. To account for the situation where the UAV reaches the ground during the turning phase, the following condition is required: if $\Delta h_{turn} > h_i$ then the aircraft cannot execute that turn, resulting in the corresponding d_x and d_y values being excluded from the FGIF.

IV. FAULT MODES AND SAFEST RESPONSE

Now that models are established for gliding flight, we next investigate the effects the four fault modes have on gliding performance.

A. Fault Modes

Faults are defined as unpermitted deviations of at least one characteristic property or parameter of the aircraft system from the acceptable or standard condition [26]. The impact of a fault can be small but it could also lead to overall system failure. After failure detection, a safe, autonomous system needs to be able to classify the fault into an appropriate category in order to mitigate its effects. Faults are classified according to where they occur in the system (i.e., sensors, actuators and other components). Faults can also be classified as abrupt, incipient, or intermittent, with respect to their time characteristics.

In this work, we consider an abrupt power system fault and combined abrupt power system/actuator faults. The actuator fault implemented in simulation consists of ailerons, rudder, and elevator surfaces stuck after a servo failure that either remain at the deflections they had at the time of the fault, or remain close to trim value [6]. It was assumed in this work that the UAV is still controllable when experiencing these faults.

1) Fault Mode 1, Engine Failure: In this fault mode, it is assumed that the UAV cannot accelerate but can change its roll, pitch and yaw angles. Because of this, the d_x and d_y in equations 21 and 22 derived above, are used in their entirety to calculate the FGIF.

2) Fault Mode 2, Engine and Rudder Failure: In this fault mode, it is assumed that the UAV cannot accelerate but can change its heading using the functioning ailerons. Even though the rudder is stuck at a specific deflection, the UAV may use its ailerons to adjust its heading. It was also assumed the aircraft's side-slip is minimal enough that it could still maneuver to various headings. The validity of this assumption is explored in Section V, where UAV trajectory and aircraft states plots are provided for the engine and rudder failure fault mode. Because of these assumptions, d_x and d_y equations derived above are used in their entirety to calculate the FGIF.

3) Fault Mode 3, Engine and Elevator Failure: In this fault mode, it is assumed that the UAV cannot accelerate or change its angle of attack, but can change its heading. The UAV's elevator is stuck at its trim value, resulting in the aircraft not having the ability to change its angle of attack. This would result in the inability of the UAV to minimize its sink rate by changing its angle of attack. Because of this, d_x and d_y equations derived above are used in their entirety to calculate the FGIF, with the limitation of not being able to change its angle of attack to reach everywhere inside the maximum FGIF boundary.

4) Fault Mode 4, Engine and Ailerons Failure: In this fault mode, it is assumed that the UAV cannot accelerate or change its heading, but can pitch. Based on our control setup, when the ailerons are stuck at trim value the UAV is unable to change its heading because heading is only controlled by the ailerons and control reconfiguration is not used in this work. If the aircraft does not have heading control, it cannot execute a turning phase. Because the UAV cannot change heading, $d\psi = 0$, which results in only straight level flight. From this, the following modified gliding flight equations must be used to reflect that only straight level gliding flight can be achieved:

$$d_x = D_{glide} sin(\frac{\pi}{2} - \psi), \tag{24}$$

$$d_y = D_{glide} cos(\frac{\pi}{2} - \psi), \tag{25}$$

$$D_{glide} = h_i \frac{v}{v_s}. \tag{26}$$

The D_{glide} term was modified to exclude the Δh_{turn} term because the aircraft is unable to turn. Notice that in the equations for d_x and d_y the $d_{x,t}$ and $d_{y,t}$ terms were removed because the aircraft is not turning while experiencing this fault mode. This results in a straight line reachable footprint. While the trajectory of an aircraft with stuck ailerons may not always be a straight line path, it is assumed in this work that ailerons are stuck close to trim value, which results in straight line trajectory.

Fig. 7 shows the FGIF of an aircraft traveling due north, experiencing Fault Mode 1 at different heights. The aircraft's initial position when experiencing the fault mode is at the origin of the plots. As the initial height of the aircraft increases, so does the FGIF (represented by the light blue shaded area of each plot). This is because the aircraft is able to glide for a longer time, resulting in a larger footprint.

Fig. 8 shows the FGIF of an aircraft traveling due north, experiencing Fault Mode 1 at different roll angles. At smaller roll angles, the aircraft cannot execute turns to larger heading angles fast enough. As a result, the aircraft cannot reach those larger angles before landing. This is seen in Fig. 8a where the aircraft experiences the fault mode while at a small roll angle. Because of this small roll angle, the FGIF is only part of a circle. As the roll angle increases, the aircraft can more quickly maneuver to larger yaw angles. This is seen in Fig. 8b and Fig. 8c where the aircraft has a larger roll angle and can reach the entire $\pm\pi$ range of yaw angles. The roll angle of the aircraft is for the turning phase of gliding flight only.
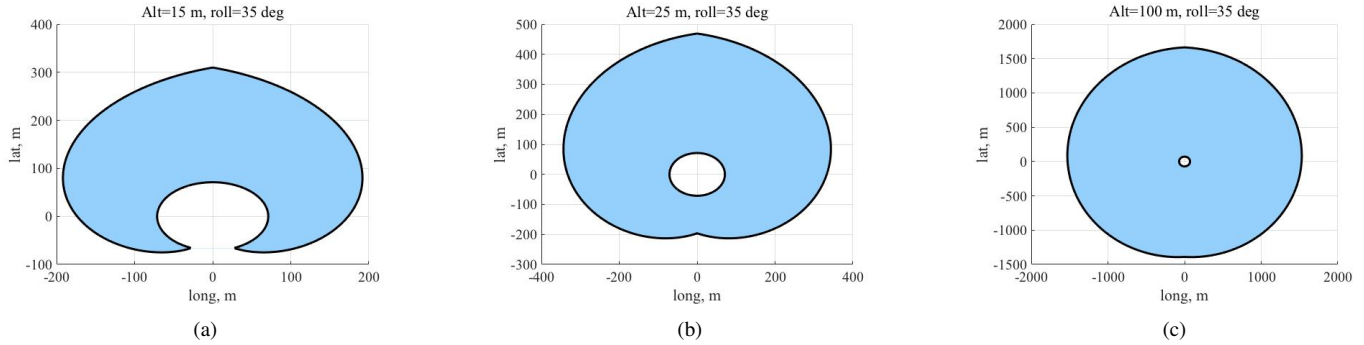
Fig. 7. Effect of aircraft height on FGIF for fault mode 1: (a) Alt=15 m, roll=35°. (b) Alt=25 m, roll=35°. (c) Alt=100 m, roll=35°. The light blue shaded area is the FGIF.
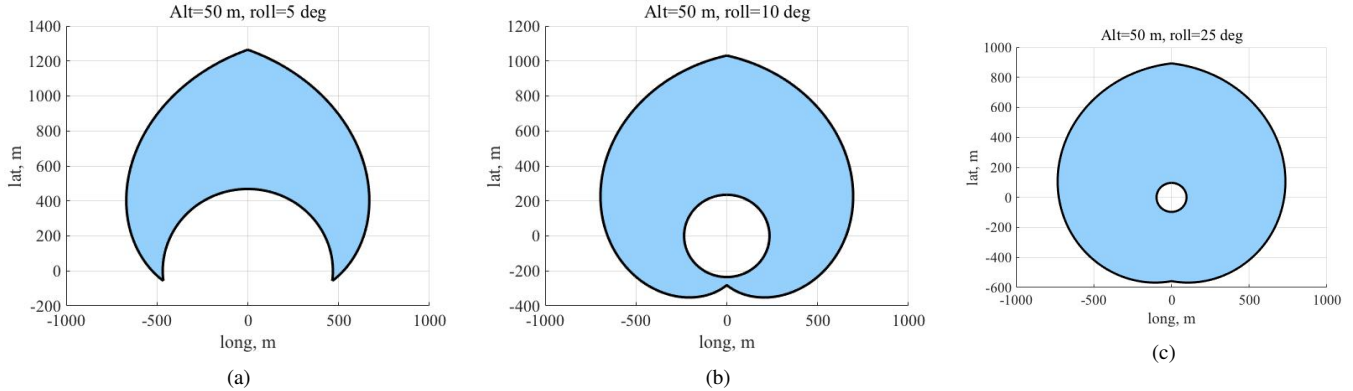

Fig. 8. Effect of aircraft roll angle on FGIF for fault mode 1: a) Alt=50 m, roll=5°. b) Alt=50 m, roll=10°. c) Alt=50 m, roll=25°. The light blue shaded area is the FGIF.

The FGIF of an aircraft experiencing the engine and rudder failure fault mode would have very similar characteristics as the engine failure fault mode. When the rudder is stuck, the ailerons are able to change the heading of the aircraft and also allow for relatively straight line flight. However, there will be side slip as a result of the rudder control being compromised. For this work, it is assumed that the side slip is minimal enough to where the aircraft can still maneuver to the calculated crash zone. The FGIF of an aircraft experiencing the engine and elevator failure fault mode would have a similar FGIF as the engine out case with the exception that the UAV can not change its angle of attack to reach anywhere inside the maximum FGIF boundary. Therefore, the FGIF would be a contour. Finally, the FGIF of an aircraft experiencing the engine and ailerons failure fault mode would be a straight line. This is because with the ailerons stuck at trim value the aircraft is unable to change its heading. However, the aircraft is able to change its angle of attack, resulting in a straight line FGIF, as opposed to a two-dimensional region.

B. Safest Response

With a model developed for the FGIF, we next develop a procedure for choosing the safest response within the reachable footprint. A searching algorithm takes the range of geodetic coordinates generated from the FGIF, and extracts all of the population values from the LandScan USA based data within the range of geodetic coordinates. It then extracts the local minimum population value for which the UAV would pose the least collective risk. The data structure of LandScan is a matrix whose rows and columns represent latitudinal and longitudinal coordinates. The value of each matrix cell is the population for that range of geodetic coordinates. [N.B. The LandScan USA dataset is restricted for use by government agencies only. We use simulated data at a 30 m resolution to show how this dataset will be integrated.]

To determine safest response, we calculate the point of lowest collective risk within the FGIF. Collective risk, also known as casualty expectation (CE), describes the aggregate risk that a UAV poses to a population of people. It is measured by expected number of casualties per flight hour [3]. Collective risk is calculated using the following equations [10]:

$$CE = PF \cdot PD \cdot AL \cdot PK \cdot S, \qquad (27)$$

$$AL = (L + DG + DS + 2B) \cdot (W + 2B). \qquad (28)$$

Definitions and the domain of variables for Eqns. 27 and 28 can be found in Table II. Probability of failure (PF) is the expected number of mishaps per flight hour, population density (PD) is the population count per square meter, probability of a fatality (PK) is the probability of a piece of the UAV striking a pedestrian and leading to a fatality, and shelter factor (S) is an estimate of how exposed a population is to falling vehicles or debris, with a factor of 0 and 1 representing completely sheltered and completely exposed, respectively. Lethal area (AL) is the area of which a fatality may occur when a vehicle or debris falls. Length (L) and width (W) refer to the wingspan and length of the aircraft, respectively, buffer (B) is a safety factor, glide distance (DG) is the distance traveled beginning

when the UAV is at an altitude of 6 ft and ending when it reaches the ground, and distance to stop (DS) is the total distance from when the UAV reaches the ground to when it comes to a complete stop. Because it is assumed that the UAV will crash and not land, $DS = 0$.

TABLE II.   Definitions of variables in casualty expectation equations.

Variable	Definition	Domain
CE	casualty expectation	[0, 6.43] fat/flt hr
P	probability of failure	(0, 1]
PD	population density per square meter	[0, 0.022] pop/m^2
AL	lethal area	77.75 m^2*
PK	probability of fatality	[0, 1]
S	shelter factor	[0, 1]
L	length	1.83 m*
W	width	1.41 m*
B	buffer	1 ft
DG	glide distance at 6 ft altitude	8.02 m*
DS	distance to stop	0 m

*Starred terms do not have a range of values because they are highly specific to the aircraft's dynamics. Representative values were given for the UAV simulated in this work.

Lethal area, length, width, glide distance, and distance to stop are all specific to the aircraft and aircraft dynamics. The upper range of population density is determined by the highest population density in the United States, located in Guttenberg, New York City. The resulting casualty expectation values can be as low as 0 fatalities per flight hour and as high as 6.43 fatalities per flight hour. For large airliners, the average casualty expectation is 0.01 fatalities per 100,000 flight hours and that of small general aviation aircraft is 0.1 fatalities per 100,000 flight hours [2]. However, the casualty expectation will be much higher than these values for UAVs because casualty expectation is proportional to probability of failure, and manned aircraft have very small probabilities of failure, 0.000064%, compared to unmanned aircraft, 2.17% [31][32]. This leads to a collective risk for small UAVs that is expected to be nearly 100,000 times larger than that of a manned aircraft.

For the purposes of this paper, probability of failure was assumed to be 0.0217, consistent with the maximum probability of failure for a small UAV defined by Sean et al. [32]. The population density was found by dividing the population count from the LandScan data by its respective area. The probability of fatality was calculated using methods explained by Range Safety Group, which was a function of the mass and speed of the aircraft [10]. A conservative shelter factor of 1 was used, representing a fully exposed population. Glide distance was calculated using the following equations [33]:

$$DG = tan(\frac{H_p}{\gamma}), \qquad (29)$$

$$\gamma = tan^{-1}(\frac{h}{d}), \qquad (30)$$

where γ is glide angle, H_p is the height of an average person and d is the ground distance traveled from when the aircraft is at height h until when it hits the ground. For calculation of CE, $h = H_p$. Note that this glide distance is different than

glide distance derived in Section III as this is the glide distance starting when the vehicle is at height H_p, not its mission plan height. By knowing the collective risk profile within the FGIF, the UAV is now able to find the point of local minimum risk and decide if the safest response is to fly to that minimum risk waypoint.

Also note that while the population data is always available, it may not always be required in determining the safest response. If the mission endpoint is within the FGIF of the aircraft then the UAV should naturally land at that waypoint as its safest response. Similarly, if the mission endpoint is not within the FGIF, but the mission start is, then the aircraft should fly back to where it started.

V. Case Study and Discussion

A. Problem Setup

With the models and algorithm logic developed, we now present a case study to show the utility of GIHM integrated with standard UAV flight control software. In this case study, we model a small fixed-wing UAV. The aerodynamic characteristics used for the small UAV are given in Table III.

TABLE III.   Characteristics of the General Aviation UAV used in simulation.

Variable	Definition	Value
v	aircraft velocity	20 m/s
α_{max}	max angle of attack	6.25°
m	maximum take off weight	1.2 kg
L_w	wingspan	1.4 m
T_w	wing taper	1.95
AR	wing aspect ratio	6.4
w_c	wing aerodynamic chord	0.22 m
$airfoil$	wing airfoil	SD7037
C_{Li}, C_{Di}, C_{Mi}	Lift, Drag, Moment coeffs. derivs.	from airfoil

The UAV's nominal mission plan contains five waypoints and a home waypoint. The waypoints approach the University of Maryland, and a given fault mode is induced into the simulation 35, 45, 65, 80, 100, and 115 seconds into the simulation. These times were chosen to obtain a wide range of flight scenarios with the UAV at different points during its mission.

Model LandScan data was created in Matlab that replicated the structure of LandScan USA data, but with a resolution of 30 m. The better resolution was required to show the utility of GIHM for small UAVs because of the size of the FGIF during simulations. Fixed blocks of higher population were created to mimic higher population expected in clusters of buildings at the University of Maryland. The dataset was preloaded into the UAV simulation and was parsed in real time when a fault mode was detected.

B. Results and Discussion

1) Casualty Expectation Reduction: This section presents numerical results for the testing of GIHM. Table IV summarizes the results of simulations for all four fault modes at six fault mode times. By examining the average casualty expectation, we can conclude that the average casualty expectation is

23.014 fatalities per 100,000 flight hours lower with the GIHM module than without the module. This equates to an 97.5% decrease in fatalities per flight hour. The percent decrease in CE with GIHM will vary depending on the magnitude of population density gradients in the area the UAV is flying. Note that the units in Table IV have units of fatalities per 100,000 flight hours, whereas CE has units of fatalities per flight hour in Table II. According to the FAA, a large airliner shall have a casualty expectation of 1 fatality per 1,000,000 flight hours, which is still far below the average casualty expectation value for the UAV with GIHM. This is because the probability of failure for this simulation is 2.17%, which is nearly 300,000 times higher than the probability of failure for a large airliner (0.000064%).

TABLE IV. Simulation results comparing CE with and without the GIHM module for all four fault modes at six different fault times. CE has units of fatalities per 100,000 flight hours.

Fault Mode	Fault Time (s)	CE With GIHM	CE Without GIHM
1	35	0.000	2.315
2	35	0.000	2.315
3	35	1.329	12.42
4	35	0.057	5.736
1	45	0.026	115.200
2	45	0.026	115.200
3	45	0.233	14.820
4	45	4.010	63.950
1	65	0.026	15.180
2	65	0.026	15.180
3	65	0.310	8.625
4	65	0.500	0.500
1	80	0.026	13.770
2	80	0.026	13.770
3	80	0.017	8.633
4	80	1.062	5.515
1	100	0.026	33.400
2	100	0.026	33.400
3	100	3.413	5.151
4	100	1.096	16.570
1	115	0.041	19.190
2	115	0.041	19.190
3	115	1.103	2.683
4	115	0.055	0.469
Average		0.584	23.598

2) UAV Mission Simulations Results With GIHM: With numerical results presented, we assume that the UAV can maneuver to and reach the low hazard waypoint provided by GIHM. This section provides the trajectory and aircraft states profiles for the simulated UAV. The trajectory and aircraft states profiles are presented for when the UAV does not experience any fault modes, and when the UAV experiences the four fault modes. These results show the limitations and maneuverability of a UAV experiencing various fault modes. They will also provide evidence that the FGIFs and low hazard waypoint provided by GIHM accurately model where the UAV can glide to.

Nominal Flight Mode: Fig. 9 and Fig. 10 show the flight simulation trajectory and altitude profile of the UAV under nominal operating conditions. The simulation terminates after
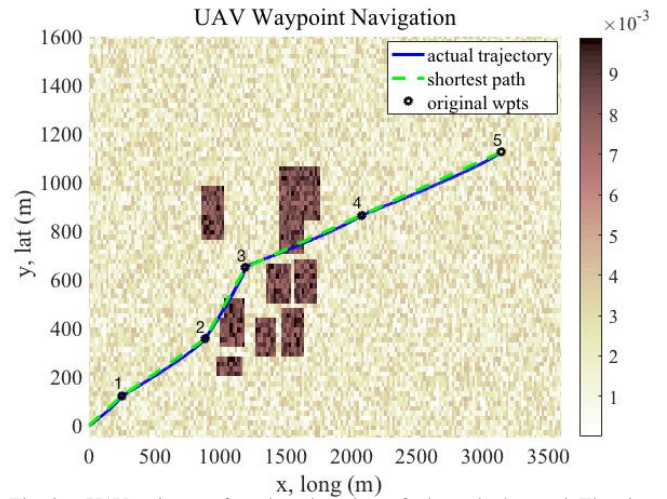

Fig. 9. UAV trajectory for when there is no fault mode detected. The aircraft starts from the home waypoint at the origin and travels to the waypoints in numerical order.
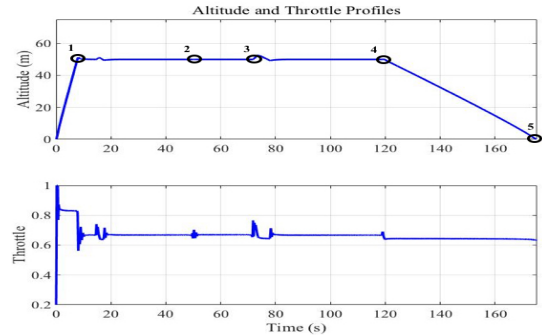

Fig. 10. UAV altitude and throttle profiles for when there is no fault mode detected. The numbered circles show the five mission waypoints. The UAV begins on the ground at the start, climbs to 50 m, then descends back to the ground when approaching waypoint 5.

the UAV reaches the fifth (final) waypoint. The trajectory plots show the relative distance the UAV travels compared to the UAV's home waypoint. On all of the trajectory plots, the heat map represents population count in that node, with darker nodes representing highly populated areas. The population heat map is pixelated as the data was generated using randomized values. The randomized values were generated based on average population values in the University of Maryland area. When LandScan USA data is used, it can easily be integrated and the heat map of the population will be smoother and more accurate. It can be seen from the trajectory plot that the actual flight path of the UAV is very close to the shortest path, indicating an effective trajectory control scheme. Fig.11 shows the Euler angle and Euler rate profiles for the nominal flight simulation. These will be used for comparison to the flight states of the UAV experiencing the various fault modes.

Now that the nominal mission plan and UAV states have been presented, we next examine how the mission plan would change when the UAV experiences different fault modes. Trajectory plots are provided for each fault mode, but UAV states and specific control surface and altitude plots were only presented for Fault Mode 2 in the interest of space, and because it provides the most interesting results.

Fault Mode 1: Fig. 12 shows the simulated flight trajectory of the UAV experiencing the engine failure (Fault Mode 1)
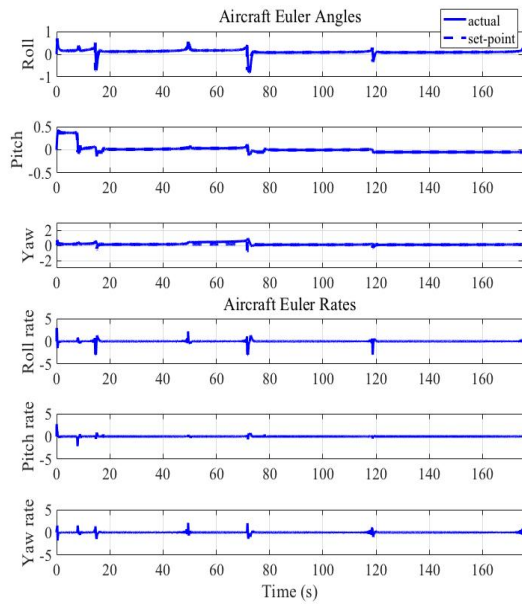
Fig. 11. UAV Euler angles and rates profiles for when there is no fault mode detected. Angles are in radians. The dashed line on the Euler angle plots show the controller commands and the solid line shows the actual aircraft states.
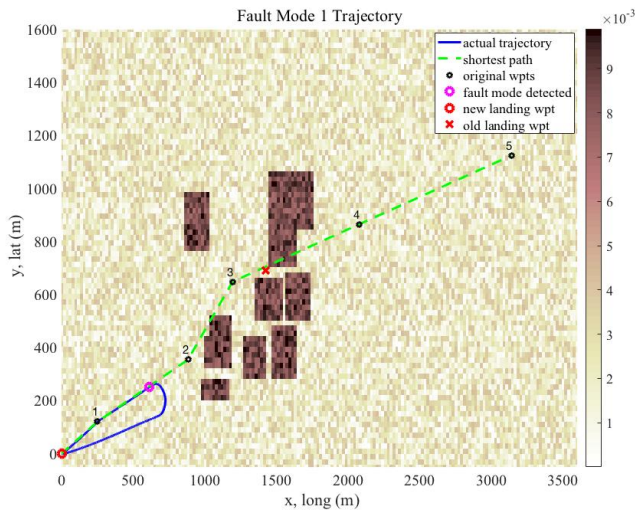

Fig. 12. UAV trajectory for when Fault Mode 1 is detected at 35 s. The aircraft starts from home at the origin and travels to the waypoints in numerical order until the fault mode is detected. New landing waypoint is the waypoint sent by GIHM and old landing waypoint is where the UAV would have landed without GIHM.

flight anomaly 35 s after mission plan initiation. This trajectory plot shows the utility of the return to base function for GIHM. When the engine failure fault mode was detected, GIHM determined that the home waypoint was within the FGIF, and the UAV was able to return home. This resulted in a casualty expectation of 0 fatalities per 100,000 flight hours, which is also reflected in Table IV.

Fault Mode 2: Fig. 13 and Fig. 14 show the simulated flight trajectory and altitude profile of the UAV experiencing the engine and rudder failure (Fault Mode 2) flight anomaly 50 s after mission plan initiation. At 50 s, as the UAV approaches waypoint 2, the engine and rudder failure fault mode is detected, which results in the change of heading and
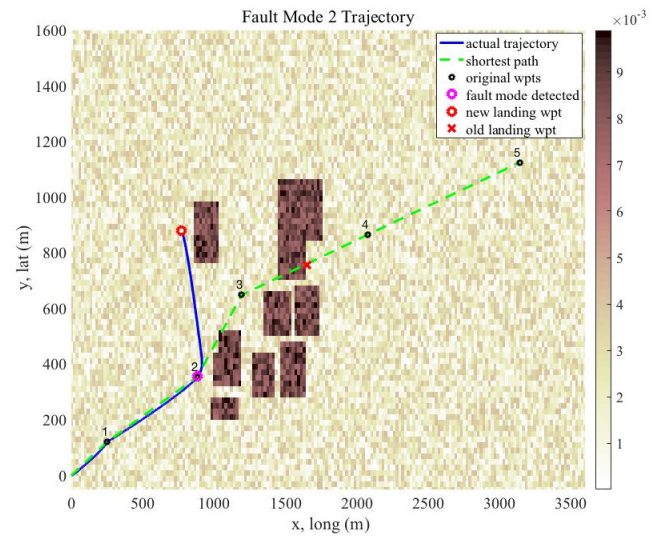

Fig. 13. UAV trajectory for when Fault Mode 2 is detected at 50 s. The aircraft starts from home at the origin and travels to the waypoints in numerical order until the fault mode is detected. New landing waypoint is the waypoint sent by GIHM and old landing waypoint is where the UAV would have landed without GIHM.

change in mission plan. To find the "old landing wpt" in Fig. 13, or where the UAV would have landed without GIHM, the simulation is run with the UAV continuing on in its initial mission plan, even when the fault is detected. The "old landing waypoint" is where the UAV is when its altitude equals zero. Fig. 14 also shows the throttle and rudder profiles of the UAV experiencing Fault Mode 2 at 50 s after mission initiation. At 50 s, the throttle is at 0 and the rudder is stuck at 0.3 radians, which are consistent with the conditions of the engine and rudder failure case. From the altitude and trajectory plots, it can be seen that the UAV found a minimum ground impact point and is flying to that point. Fig. 13 shows where the UAV would have landed compared to where it was able to maneuver. The new landing waypoint is in a less populated spot compared to the old landing point. A safety factor of 30 m was included to ensure the UAV does not land adjacent to the highly populated cluster of buildings. Fig. 13 shows that sideslip is minimal when the rudder is stuck and that the ailerons are sufficient in guiding the aircraft to the low hazard waypoint. Fig. 15 shows the Euler angles and Euler rates for the UAV experiencing Fault Mode 2 50 s after flight initiation. Note the change in Euler angles at time 50 s, which is a result of the aircraft changing heading to fly to the new priority waypoint generated by GIHM.

Fault Mode 3: Fig. 16 shows the simulated flight trajectory of the UAV experiencing the engine and elevator failure (Fault Mode 3) flight anomaly 80 s after mission plan initiation. The trajectory plot shows the UAV maneuvering to the lowest hazard waypoint, as opposed to continuing on its mission plan. If it continued on in its mission, the casualties per flight hour would have been much higher because it would have landed in a much higher populated area.

Fault Mode 4: Fig. 17 shows the simulated flight trajectory of the UAV experiencing the engine and ailerons failure (Fault Mode 4) flight anomaly 45 s after mission plan initiation. The
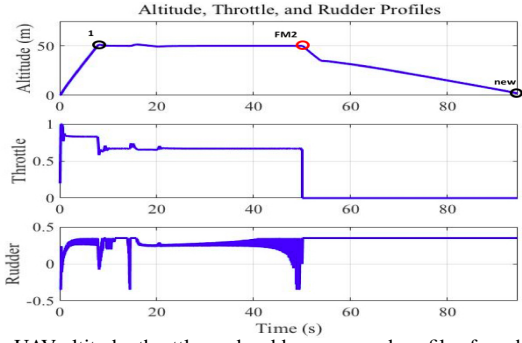
Fig. 14. UAV altitude, throttle, and rudder command profiles for when Fault Mode 2 is detected at 50 s. The numbered circles show the mission waypoints, with the one labeled 'new' representing the new landing waypoint generated by GIHM. The red circle represents when the fault mode was detected. The aircraft starts on the ground, climbs to reach waypoint 1, then descends when the fault mode is detected at 50 s.
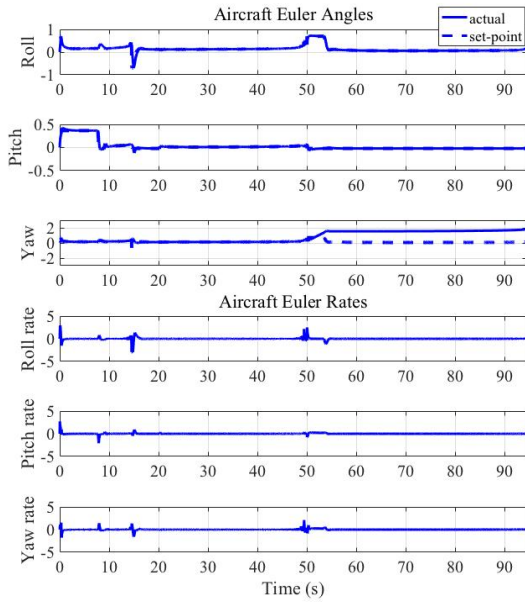

Fig. 15. UAV Euler angles and rates profiles for when Fault Mode 2 is detected at 50 s. Angles are in radians. The dashed line on the Euler angle plots show the controller commands and the solid line shows the actual aircraft states. The aircraft has changes in all three Euler angles when the fault mode is detected at 65 s because of the maneuvers made by the UAV to reach the safest landing point.

trajectory plot shows that even when the ailerons are stuck at trim value, the aircraft is still able to fly in a straight line path and change its elevator deflection to reach the lowest hazard waypoint. If the UAV continued on its nominal mission plan then it would have ended up flying over and crashing in a highly populated area.

These fault scenarios were setup such that the UAV would have had an emergency descent to an area of higher population density. In all the fault modes studied, it was shown that after detection of a fault mode, GIHM calculated the lowest casualty expectation impact waypoint and was able to maneuver to that point. The new waypoints for all trajectory plots successfully avoided the highly populated areas, while the aircraft could have landed on the edge of the highly populated zones if the UAV had not used the GIHM module. It was observed that fault modes that allow for heading changes require more com-
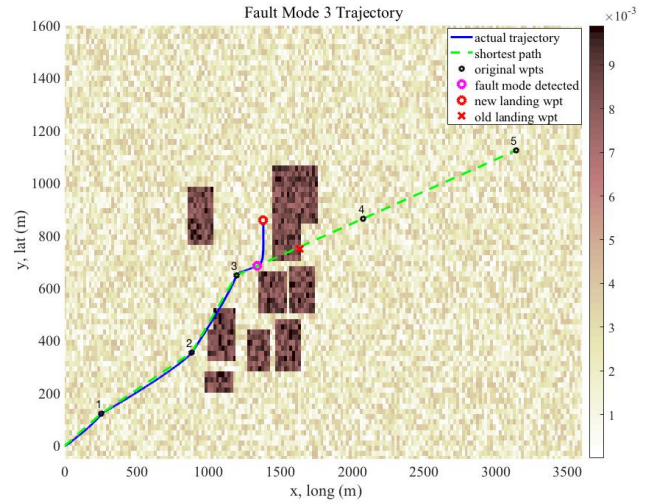

Fig. 16. UAV trajectory for when Fault Mode 3 is detected at 80 s. The aircraft starts from home at the origin and travels to the waypoints in numerical order until the fault mode is detected. New landing waypoint is the waypoint sent by GIHM and old landing waypoint is where the UAV would have landed without GIHM.
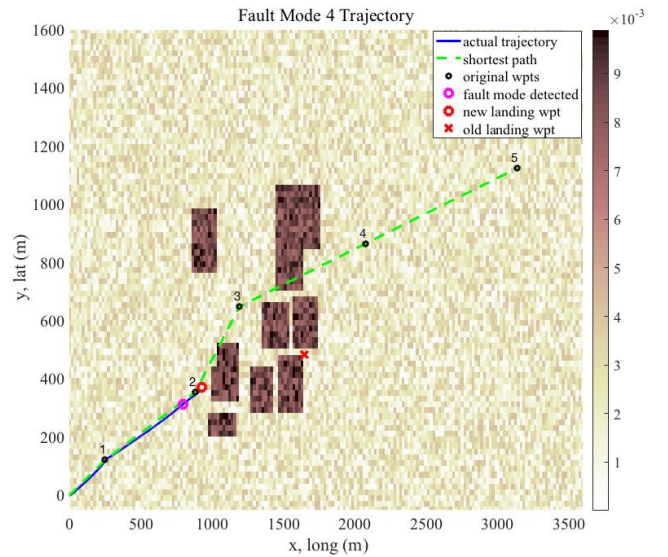

Fig. 17. UAV trajectory for when Fault Mode 4 is detected at 45 s. The aircraft starts from home at the origin and travels to the waypoints in numerical order until the fault mode is detected. New landing waypoint is the waypoint sent by GIHM and old landing waypoint is where the UAV would have landed without GIHM.

putation time because of the added amount of data points in the FGIF. The design of the GHIM module allows for real-time implementation of safe reactions to anomalies. Computation time for the GIHM module ranges between 0.01 s and 0.04 s on a 2015 MacBook Air with 1.6 GHz I5 processor, depending on which fault mode the UAV is in.

VI. CONCLUSION

Understanding the footprint for a UAV experiencing flight anomalies is an important first step in safer UAV control software. However, existing ground footprint models for UAV decision making either do not take into account population density in the reachable footprint, or the population density

data accuracy needs to be improved. The addition of a precise population dataset is an important addition to reachable ground footprint models because the UAV now possesses the ability to quantify its ground impact after determining where it can land.

This work combined a reachable ground footprint model with a precise synthetic population dataset with Landscan USA data properties, all while integrating the module with a flight simulation software that included a 6-DOF aircraft model, path planning, and autopilot control. For our mission configuration and population profile, this work successfully decreased the casualty expectation of a small UAV by an average of 23.014 fatalities per 100,000 flight hours, or a 97.5% decrease in casualty expectation. The development of the fault modes allowed for a basis of investigation into where a UAV might land given the restrictions that specific fault modes cause and how the UAV can reduce casualty expectation for different flight anomalies.

Future work includes examining how uncertainties in different UAVs and environment parameters may affect the performance of GIHM, developing fault modes for accelerated aircraft experiencing various control surface malfunctions, integrating a collision detection and avoidance module, addition of topology data for landing site considerations, and a more sophisticated decision making engine that allows the UAV to execute various flight control instability mitigation maneuvers during flight anomalies before diagnosing a fault mode.

Acknowledgment

References

[1] H. Chen, X.-m. Wang, and Y. Li, "A survey of autonomous control for uav," in *Artificial Intelligence and Computational Intelligence, 2009. AICI'09. International Conference on*, vol. 2. IEEE, 2009, pp. 267–271.

[2] R. Loh, Y. Bian, and T. Roe, "Uavs in civil airspace: safety requirements," *IEEE A&E Systems Magazine*, vol. 24, no. 1, pp. 5–17, 2009.

[3] P. P. Wu and R. A. Clothier, "The development of ground impact models for the analysis of the risks associated with unmanned aircraft operations over inhabited areas," in ***Proceedings of the 11th probabilistic safety assessment and management conference (PSAM11) and the annual European safety and reliability conference (ESREL 2012)***, 2012.

[4] B. Elias, "Pilotless drones: Background and considerations for congress regarding unmanned aircraft operations in the national airspace system," *Congressional Research Service Washington DC*, 2012.

[5] N. Neogi, K. Bhamidipati, D. Uhlig, A. Ortiz, and J. Krauss, "Engineering safety and reliability into uav systems: mitigating the ground impact hazard," in *AIAA Guidance, Navigation and Control Conference and Exhibit*, 2007, p. 6510.

[6] C. M. Belcastro, D. H. Klyde, M. J. Logan, R. L. Newman, and J. V. Foster, "Experimental flight testing for assessing the safety of unmanned aircraft system safety-critical operations," in *17th AIAA Aviation Technology, Integration, and Operations Conference*, 2017, p. 3274.

[7] W. Schneider, "Defence science board study on unmanned aerial vehicles and uninhabited combat aerial vehicles," *US Department of Defence, Tech. Rep*, 2004.

[8] R. Venkataraman, M. Lukátsi, B. Vanek, and P. Seiler, "Reliability assessment of actuator architectures for unmanned aircraft," *IFAC-PapersOnLine*, vol. 48, no. 21, pp. 398–403, 2015.

[9] C. Lum and B. Waggoner, "A risk based paradigm and model for unmanned aerial systems in the national airspace," in *Infotech@ Aerospace 2011*, 2011, p. 1424.

[10] R. C. Council, "Range safety criteria for unmanned air vehicles," *Series Range Safety Criteria for Unmanned Air Vehicles. White Sands Missile Range, NM: Range Safety Group of the Range Commander's Council at the White Sands Missile Range*, 1999.

[11] D. Burke, C. Hall, and S. Cook, "System-level airworthiness tool," in *Journal of Aircraft*, 2011, pp. 777–785.

[12] J. Stevenson, S. O'Young, and L. Rolland, "Estimated levels of safety for small unmanned aerial vehicles and risk mitigation strategies," in *Journal of Unmanned Vehicle Systems*, 2015, pp. 205–221.

[13] R. Clothier, R. Walker, N. Fulton, and D. Campbell, "A casualty risk analysis for unmanned aerial system (uas) operations over inhabited areas," in *Second Australasian Unmanned Air Vehicle Conference*, 2007, pp. 1–15.

[14] J. W. Herrmann and S. Azarm, "Risk-based path planning optimization methods for unmanned aerial vehicles over inhabited areas," *algorithms*, vol. 12, p. 13, 2016.

[15] A. Washington, R. A. Clothier, and J. Silva, "A review of unmanned aircraft system ground risk models," *Progress in Aerospace Sciences*, vol. 95, pp. 24–44, 2017.

[16] M. Coombes, W.-H. Chen, and P. Render, "Reachability analysis of landing sites for forced landing of a uas," *Journal of Intelligent & Robotic Systems*, vol. 73, no. 1-4, pp. 635–653, 2014.

[17] N. Bradley and D. Burke, "Potential crash location (pcl) model," Naval Air Warfare Center Aircraft Div Patuxent River MD, Tech. Rep., 2012.

[18] E. Atkina, I. Portillo, and M. Strube, "Emergency flight planning applied to total loss of thrust," *Journal of Aircraft*, pp. 1205–1216.

[19] L. Barr, R. Newman, E. Ancel, C. Belcastro, J. Foster, J. Evans, and D. Klyde, "Preliminary risk assessment for small unmanned aircraft systems," in *17th AIAA Aviation Technology, Integration, and Operations Conference*, 2017, p. **3272**.

[20] B. Bhaduri, E. Bright, P. Coleman, and M. Urban, "Landscan usa: a high-resolution geospatial and temporal modeling approach for population distribution and dynamics," *GeoJournal*, vol. 69, pp. 103–117, 2007.

[21] X. Li, R. Rowley, J. Kostelnick, D. Braaten, J. Meisel, and K. Hulbutta, "Gis analysis of global impacts from sea level rise," *Photogrammetric Engineering and Remote Sensing*, vol. 75, no. 7, pp. 807–818, 2009.

[22] P. Sutton, C. Elvidge, and T. Obremski, "Building and evaluating models to estimate ambient population density," *Photogrammetric Engineering and Remote Sensing*, vol. 69, no. 5, pp. 545–553, 2003.

[23] C. Linard and A. J. Tatem, "Large-scale spatial population databases in infectious disease research," *International journal of health geographics*, vol. 11, no. 1, p. 7, 2012.

[24] A. Poissant, L. Castano, and H. Xu, "Ground impact and hazard mitigation for safer uav flight response," in *International Conference on Unmanned Aircraft Systems*, 2018.

[25] C. Bogdiukiewicz, M. Butler, T. S. Hoang, M. Paxton, J. Snook, X. Waldron, and T. Wilkinson, "Formal development of policing functions for intelligent systems," pp. **194–204**, 2017.

[26] M. Verhaegen, S. Kanev, R. Hallouzi, C. Jones, J. Maciejowski, and H. Smail, "Fault tolerant flight control-a survey," in *Fault tolerant flight control*. Springer, 2010, pp. 47–89.

[27] M. Azam, K. Pattipati, J. Allanach, S. Poll, and A. Hine, "In-flight detection and isolation in aircraft flight control systems," in *IEEE Aerospace Conference*, March 2005.

[28] F. Irving, *The paths of soaring flight*. World Scientific, 1999.

[29] J. D. Anderson, *Fundamentals of aerodynamics*. McGraw-Hill Companies, 1984.

[30] T. R. Yechout, *Introduction to aircraft flight mechanics*. Aiaa, 2003.

[31] Boeing, *Statistical Summary of Commercial Jet Airplane Accidents*, accessed December 1, 2018. [Online]. Available: http://www.boeing.com/resources/boeingdotcom/company/about_bca/pdf/statsum.pdf

[32] S. E. Wolf, "Modeling small unmanned aerial system mishaps using logistic regression and artificial neural networks," Air Force Inst of Tech Wright-Patterson AFB OH, Tech. Rep., 2012.

[33] M. H. Sadraey, *Aircraft Performance: An Engineering Approach*. CRC Press, 2017.